Jiahui Ye[1]
Wm Michael Barnes'64
Department of Industrial and
Systems Engineering,
Texas A&M University,
College Station, TX 77843
e-mail: jhy@tamu.edu

Mohamad Mahmoudi[1]
Wm Michael Barnes'64
Department of Industrial and
Systems Engineering,
Texas A&M University,
College Station, TX 77843

Kubra Karayagiz
Department of Material Science & Engineering,
Texas A&M University,
College Station, TX 77843

Luke Johnson
Department of Material Science & Engineering,
Texas A&M University,
College Station, TX 77843

Raiyan Seede
Department of Material Science & Engineering,
Texas A&M University,
College Station, TX 77843

Ibrahim Karaman
Department of Material Science & Engineering,
Texas A&M University,
College Station, TX 77843

Raymundo Arroyave
Department of Material Science & Engineering,
Texas A&M University,
College Station, TX 77843

Alaa Elwany[2]
Wm Michael Barnes'64
Department of Industrial and
Systems Engineering,
Texas A&M University,
College Station, TX 77843
email: elwany@tamu.edu

Bayesian Calibration of Multiple Coupled Simulation Models for Metal Additive Manufacturing: A Bayesian Network Approach

Modeling and simulation for additive manufacturing (AM) are critical enablers for understanding process physics, conducting process planning and optimization, and streamlining qualification and certification. It is often the case that a suite of hierarchically linked (or coupled) simulation models is needed to achieve the above tasks, as the entirety of the complex physical phenomena relevant to the understanding of process-structure-property-performance relationships in the context of AM precludes the use of a single simulation framework. In this study using a Bayesian network approach, we address the important problem of conducting uncertainty quantification (UQ) analysis for multiple hierarchical models to establish process-microstructure relationships in laser powder bed fusion (LPBF) AM. More significantly, we present the framework to calibrate and analyze simulation models that have experimentally unmeasurable variables, which are quantities of interest predicted by an upstream model and deemed necessary for the downstream model in the chain. We validate the framework using a case study on predicting the microstructure of a binary nickel-niobium alloy processed using LPBF as a function of processing parameters. Our framework is shown to be able to predict segregation of niobium with up to 94.3% prediction accuracy on test data.
[DOI: 10.1115/1.4052270]

Keywords: metal additive manufacturing, laser powder bed fusion, uncertainty quantification, Bayesian network, calibration, Gaussian process, nickel-niobium alloy

1 Introduction

Metal additive manufacturing (AM) processes are known for a broad spectrum of attractive capabilities, such as a high degree of geometric complexity, the ability to customize parts, and material saving through design and topology optimization. Other emerging capabilities of AM continue to evolve, including the potential of producing parts with tailored spatially varying properties, commonly known as functional grading [1,2]. Laser powder bed fusion (LPBF) is a common AM process that produces physical objects directly from a digital computer model through selectively fuzing raw powder particles using a high energy laser beam [3]. Commercial LPBF technologies include selective laser sintering for processing polymeric powders, and selective laser melting or direct metal laser sintering for processing metallic powders [4]. Our focus in this study is on metal LPBF, which has been shown to successfully build nearly fully dense parts using a variety of metallic materials and alloys including stainless steels [5–8], titanium alloys [9,10], thermoelectric materials [11], nickel-based super alloys [12], and shape memory alloys [13–18].

Although LPBF processes offer attractive capabilities, they also come with their own challenges including the elevated cost and time involved in the processes task of material and part qualification and certification (Q&C) [19–21]. To streamline Q&C, researchers and practitioners have attempted different approaches. One approach is through process monitoring and control (see

[1]Jiahui Ye and Mohamad Mahmoudi contributed equally to this paper.
[2]Corresponding author.
Manuscript received February 10, 2021; final manuscript received August 17, 2021; published online October 14, 2021. Assoc. Editor: Zhen Hu.

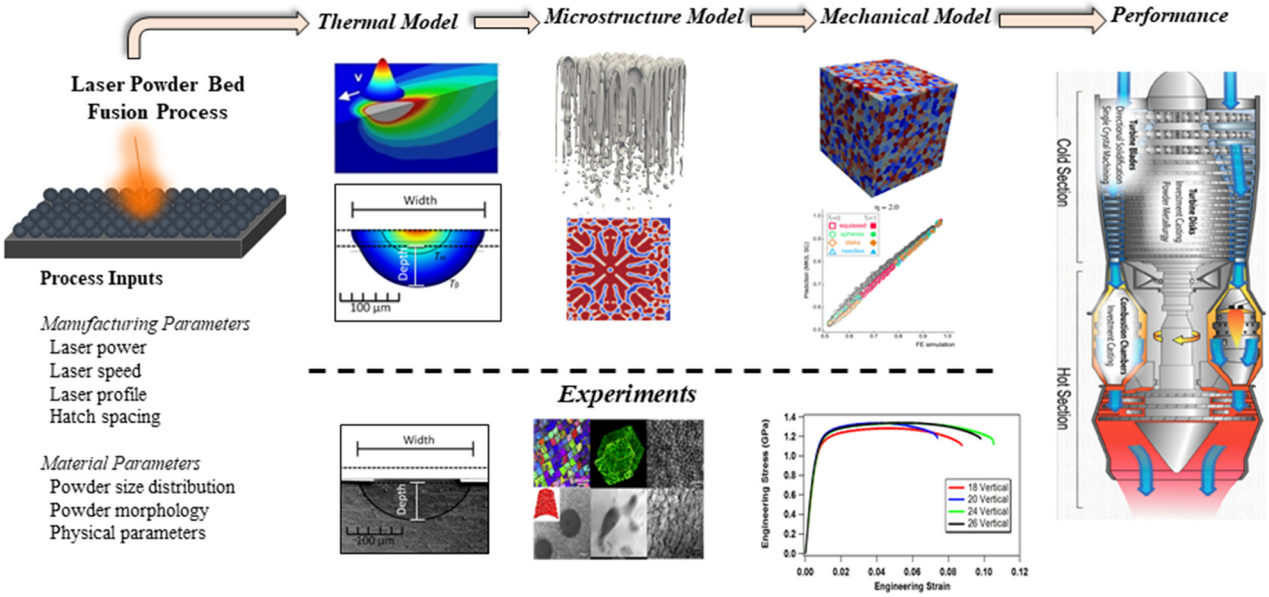

Fig. 1 Schematic of a network of integrated computational material models for LPBF and corresponding validation experiments

[22–25]). Another approach, which is the focus of this paper, is through AM modeling and simulation. This involves the development of physics-based computer simulation models based on first principles, i.e., fundamental physics-based frameworks as opposed to nonparametric models, and the understanding of underlying physics of the process (see, for example, Refs. [26–29]). Such models are very useful for achieving many objectives including identifying sources of process variability, understanding defect formation mechanisms, and predicting part microstructure and properties, among many others.

Since LPBF (and metal AM in general) is a complex process that involves multiple complex physical mechanisms, such as very rapid solidification and remelting, a framework is needed that leverages multiscale and multiphysics modeling for better analysis and understanding of the process. Hence, metal AM is an area that can benefit substantially from the field of integrated computational materials engineering (ICME). By definition, ICME prescribes a framework for accelerating the development and deployment of materials through the establishment and exploitation of process–structure–property–performance (PSPP) relationships. PSPP in turn can be established through linking material models at multiple scales. The goal in ICME is to optimize the materials, manufacturing process, and component designs before part fabrication [30]. Figure 1 shows a schematic of a network of integrated computational material models used in LPBF. Ideally, the network can be utilized to predict the performance of a LPBF part using multiple simulation models that are linked through their input and output variables.

ICME models use governing physical equations to predict specific quantities of interest (QoIs). As a well-established fact, all of these models are imperfect and thus their predictions will deviate from the actual physical phenomena they are meant to describe [31]. The disagreement between the real-world and the model outputs can be attributed to one or more of the following factors: (1) incomplete understanding of the underlying physical phenomena, (2) incomplete or inaccurate information about model parameters, (3) incorrect values for the model inputs, (4) natural stochastic behavior of the system, and (5) uncertainties associated with available numerical algorithms [30,32–35]. Hence, conducting rigorous uncertainty quantification (UQ) analysis of these physics-based models using experimental observations becomes a vital task. In addition to UQ, sensitivity analysis (SA) also plays an important role in uncertainty analysis. Via quantifying the relative importance of each model input with respect to QoIs, SA seeks to identify significant model inputs and improve understanding of the PSPP processes especially the relationships between inputs and QoIs. Therefore, in this study to complete the uncertainty analysis, SA is conducted after rigorous UQ.

One example of problem that is addressed within the field of UQ is the statistical calibration problem. This problem refers to making inferences on the set of input parameters whose values are unknown at the time of running the simulations such that model predictions are in agreement with experimental observations [36]. Such input parameters are usually known as calibration parameters. The body of literature on the statistical calibration of a single simulation model is quite rich, with many significant applications of the Bayesian framework by Kennedy and O'Hagan [37], Conti and O'Hagan [38], and Higdon et al. [39]. While calibrating a single model is very useful for many applications, when it comes to effective deployment of ICME in metal AM, it is almost always the case that the task under consideration is described by a system (or a network) of simulation models rather than a single model. This is particularly true in the case of LPBF, as illustrated in Fig. 1. Although we can easily find study efforts of UQ for a complex system with multiple linked simulation models (see, for example, Refs. [40–44]), there are only a limited number of research studies in the field of AM (see, for example, Refs. [45,46]). Currently, most AM case studies are still for single-level surrogate model calibration, for example, physics-based precipitation model calibration for nickel–titanium shape memory alloy in Ref. [14], and the thermal model calibration for Ti-6Al-4V in Ref. [47] and AF9628 in Ref. [48]. Furthermore, most prior works on statistical calibration deal with single scalar output models. For the case of ICME in metal AM, the models may have multiple QoIs, which are all essential to gain a useful understanding of process-structure–property–performance relationships, and multivariate calibration in AM is discussed in Ref. [47]. To complicate matters, even more, portions of these QoIs are often unmeasurable, i.e., no direct experimental measurements can be acquired for purpose of validation and calibration.

In this work, we address the challenges outlined above. More specifically, we conduct rigorous UQ analysis for a network of hierarchically connected (or coupled) ICME models needed to establish PSPP relationships in the metal LPBF process. We

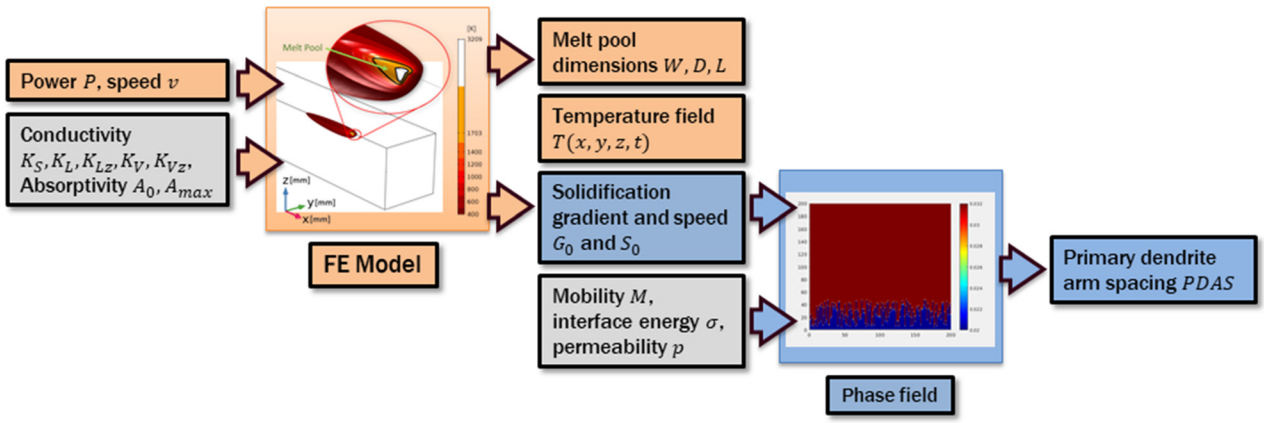

Fig. 2 Relationships between two coupled models in AM

present a framework to enable effective UQ and calibration of these models in the challenging case when no experimental observations for one or more QoIs—that may serve as inputs to the next element of the model chain—are available. Such lack of experimental data can either be attributed to technological limitations or due to cost consideration. For example, thermal gradients in the processed material are outputs of one of the models which are extremely difficult to measure. In our proposed framework, we first use a Bayesian network to model the relationships and interactions between the linked simulation models and their variables. Next, we use the Gaussian process to build surrogate models and then use a Bayesian scheme to conduct parameter calibration. To evaluate the performance of the proposed framework, a case study of hierarchically linked ICME models for LPBF is conducted using the binary nickel-niobium (NiNb) alloy.

The remainder of this paper is organized as follows: Sec. 2 introduces the physics-based models in this study: Sec. 2.1 describes the finite element thermal model and Sec. 2.2 describes the phase field microstructure model. Section 3 illustrates the framework for the calibration of multiple coupled models. Section 4 shows the process and results of implementing the proposed framework for the NiNb alloy. Section 5 concludes the paper with a summary of findings.

2 Hierarchical Physics-Based Models

The coupled models in this study start with a finite element thermal model (FETM) (also referred to as the melt pool model throughout this paper) as the upstream model. The melt pool refers to the interface between the laser beam and the metallic powder being processed. This model establishes the linkage between the AM manufacturing processing parameters and the resulting thermal history during fabrication. A portion of the outputs of this model is used as inputs to the downstream phase field (PF) microstructure model. Figure 2 schematically shows the relationships between the variables of each of these two models. Given a set of process parameters, laser power and speed, the FETM predicts useful quantities including melt pool dimensions, melt pool temperature, solidification gradient, and solidification speed at different locations along the melt pool surface. Given the solidification gradient and solidification speed at a particular location, the PF model predicts QoIs representing microstructural features. In particular, the main QoI of coupled models in this work is the primary dendrite arm spacing (PDAS), denoted by λ, which is of great importance when studying the microstructure of an additively manufactured part. Sections 2.1 and 2.2 overview the FETM and the PF model separately. More details about the models are discussed in Ref. [49].

2.1 The Finite Element Thermal Model. This model is based on a three-dimensional FETM developed by the coauthors in previous work [49]. The model is implemented in COMSOL MULTIPHYSICS heat transfer module to study melt pool characteristics, including geometry and thermal profiles, during LPBF. It includes phase-dependent thermophysical properties which are used to approximate heat and mass transport phenomena such as melting, solidification, vaporization, and keyhole formation. The powder layer is assumed to be a 30 μm continuum medium over a 1 mm thick Ni-5 wt %Nb alloy substrate.

Note that in this work, not only are we using the FETM to predict melt pool dimensions and peak temperatures as reported in Ref. [50], but also we are computing the solidification gradient and solidification speed (denoted by G and S, respectively) for every point on the surface of the melt pool. A representative output of the FETM that shows G and S is shown in Fig. 3 where the solidification gradient and speed are evaluated across the entire melt pool boundary and color coded. Both of these quantities (G and S) are symmetric about the laser scan path. Hence, for a specific point such as the solidification tail indicated in the figure, we can report temperature, solidification gradient, and solidification speed. We denote these three values by T_0, G_0, and S_0, respectively. We can specify the entire FETM model by defining three vectors : (1) control inputs $\boldsymbol{x}_1$, (2) model parameters $\boldsymbol{\theta}_1$, and (3) model outputs $\boldsymbol{y}_1$. These vectors are described in detail in Table 1.

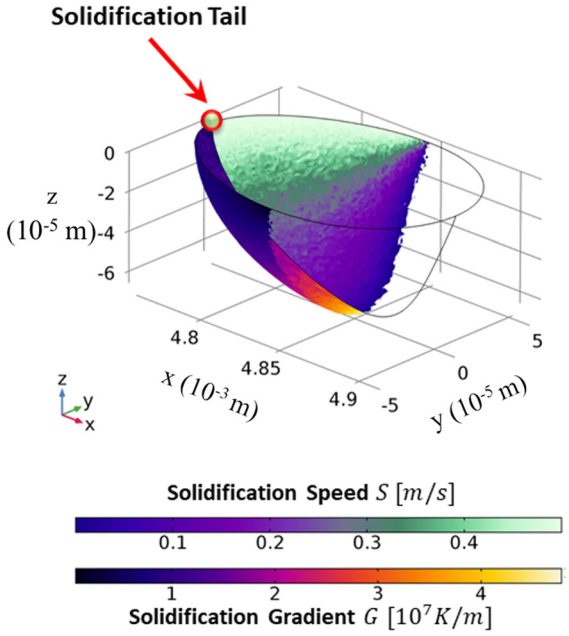

Fig. 3 Sample output of the FETM showing the solidification gradient and solidification speed along the surface of the melt pool

Table 1 Specifications of the FETM

The melt pool model, $\mathcal{M}_1$	
Variable summary	
$\boldsymbol{x}_1 = [P, v]^T$	
$\boldsymbol{\theta}_1 = [K_S, K_L, K_{Lz}, K_V, K_{Vz}, A_0, A_{max}]^T$	
$\boldsymbol{y}_1 = [D, W, L, T_0, S_0, G_0]^T$	
Control inputs, $\mathbf{x}_1$	
P: Laser power	(W)
v: Laser speed	(m/s)
Model parameters, $\boldsymbol{\theta}_1$	
K_S: Thermal conductivity coefficient solid	(W/mK)
K_L: Thermal conductivity coefficient liquid	(W/mK)
K_{Lz}: Anisotropic thermal conductivity coefficient liquid	(W/mK)
K_V : Thermal conductivity coefficient vapor	(W/mK)
K_{Vz}: Anisotropic thermal conductivity coefficient vapor	(W/mK)
A_0: Bulk absorptivity of powder	
A_{max}: Max absorptivity of powder	
Outputs, $\mathbf{y}_1$	
D: Melt pool depth	(μm)
W : Melt pool width	(μm)
L: Melt pool length	(μm)
T_0: Temperature	(K)
S_0: Solidification speed	(m/s)
G_0: Solidification gradient	(K/m)

As shown in Sec. 2.2, portions of the model outputs are used as inputs to the PF microstructure model.

2.2 The Phase Field Microstructure Model. A phase-field model is used to investigate the solidification microstructure of AM parts. This is a powerful technique for describing complex microstructural evolutions without needing to track the moving interface, as opposed to classical sharp interface models. By hierarchically coupling the PF model with the FETM at the solidification tail shown in Fig. 3, quantifiable predictions of solidification phenomena during LPBF can be achieved.

In this work, we adopt the PF model with finite interface dissipation introduced by Steinbach et al. [51] and Zhang and Steinbach [52] to investigate the rapid solidification process during LPBF of Ni-5 wt %Nb (Ni-3.2at %Nb) alloy. The model is capable of describing the extreme nonequilibrium conditions that prevail in rapid solidification during AM. At its heart, the present implementation of the PF model uses the finite difference method to numerically solve the following phase-field and concentration evolution equations:

$$\phi_\alpha c'_\alpha = \nabla(\phi_\alpha D_\alpha \nabla c_\alpha) + p^{\text{int}}\phi_\alpha\phi_\beta\left(\frac{\partial f_\beta}{\partial c_\beta} - \frac{\partial f_\alpha}{\partial c_\alpha}\right) + \phi_\alpha\phi'_\alpha(c_\beta - c_\alpha) \tag{1}$$

$$\phi_\beta c'_\beta = \nabla(\phi_\beta D_\beta \nabla c_\beta) + p^{\text{int}}\phi_\alpha\phi_\beta\left(\frac{\partial f_\alpha}{\partial c_\alpha} - \frac{\partial f_\beta}{\partial c_\beta}\right) + \phi_\beta\phi'_\beta(c_\alpha - c_\beta) \tag{2}$$

$$\phi'_\alpha = K\left\{\sigma_{\alpha\beta}\left[\nabla^2\phi_\alpha + \frac{\pi^2}{\eta^2}\left(\phi_\alpha - \frac{1}{2}\right)\right] - \frac{\pi^2}{8\eta}\Delta g^\phi_{\alpha\beta}\right\} \tag{3}$$

$$K = \frac{8p^{\text{int}}\eta\mu_{\alpha\beta}}{8p^{\text{int}}\eta + \mu_{\alpha\beta}\pi^2(c_\alpha - c_\beta)^2} \tag{4}$$

$$\Delta g^\phi_{\alpha\beta} = f_\alpha - f_\beta + \left(\phi_\alpha\frac{\partial f_\alpha}{c_\alpha} - \phi_\beta\frac{\partial f_\beta}{c_\beta}\right)(c_\beta - c_\alpha) \tag{5}$$

In the above equations, $\sigma_{\alpha\beta}$, η, $\phi_{\alpha/\beta}$, $c_{\alpha/\beta}$, and c are the interfacial energy, the interface width, the phase fractions of α/β phases, the phase concentrations of α/β phases, and the overall concentration, respectively. D_α and D_β are the chemical diffusivities in the α and β phases, respectively, and p^{int} is the interface permeability defined as $p^{\text{int}} = 8M/(a\eta)$. M is the atomic mobility and a is the lattice constant. $\mu_{\alpha\beta}$ is the interfacial mobility, K is the kinetic coefficient describing the effect of finite diffusion and redistribution at the interface, and $\Delta g^\phi_{\alpha\beta}$ is the chemical driving force. Further information on the physical meaning of the interface permeability, p^{int}, can be found in the referenced paper [51].

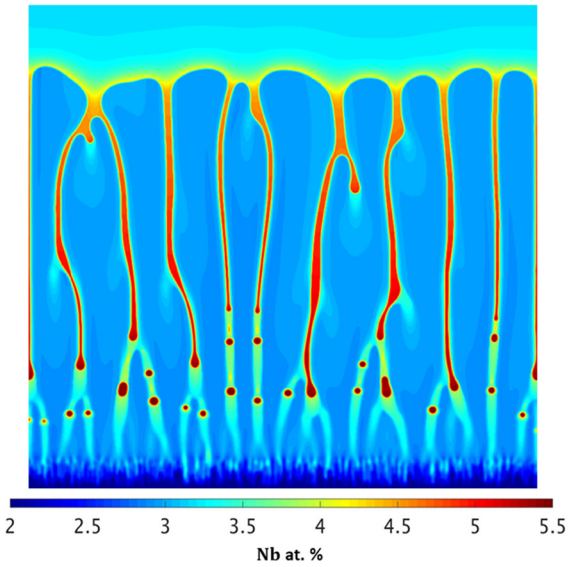

Fig. 4 Sample output of the phase field model

A dynamic time-step is adopted in this work to ensure numerical stability as explained in Ref. [49]. Neumann boundary conditions are applied to all boundaries, which specify the derivatives at the boundaries of the domain to be constants. The initial simulation domain consists of a thin layer of FCC-γ solid at the bottom and a thick layer of liquid on the top, to promote cellular segregation structure random perturbations are applied to the solid–liquid interface. Initial Nb compositions of the solid and liquid are set to $c_s^0 = c_s^{\text{eq}} = 2.2(\text{at}\,\%\text{Nb})$ at $T = T_0 = 1695\,K$ and $c_l^0 = c_{\text{alloy}} = 3.2(\text{at}\,\%\text{Nb})$.

A Fortran code with OpenMP parallelization directives is utilized to reduce the computational time. To investigate the general features of the microstructure, a two-dimensional simulation domain with the size of $616\Delta x$ by $4500\Delta y$ is used, where the grid spacing $\Delta x = \Delta y = 0.004\,\mu$m in our case. To study the effect of process parameters, a domain size of $800\Delta x$ by 800 Δy is used. At the solidification tail, we assume PDAS reaches its steady-state, where the cell tips advance at a constant velocity and hence S_0 assumed constant over the PF model domain. To account for the varying temperature during the solidification process, the frozen temperature approach is applied, which neglects the latent heat released during solidification and assumes G_0 to be constant in the domain of the PF model. Figure 4 shows a representative output of the PF model. Similar to the melt pool model, we can specify the phase field model by defining three vectors: (1) control inputs $\mathbf{x}_2$, (2) model parameters $\boldsymbol{\theta}_2$, and (3) outputs $\mathbf{y}_2$. These vectors are described in detail in Table 2.

To help readers better understand how the two models are hierarchically coupled, we summarize the procedure as follows: consider that we are interested in analyzing the microstructure of the solidification tail shown in Fig. 3 for a specific set of LPBF process parameters (laser power P and laser speed v). The process parameters constitute the input vector $\mathbf{x}_1$ as described in Table 1. Once $\mathbf{x}_1$ is set, we can use the trained Gaussian process (GP) surrogate model and input $\mathbf{x}_1$ and $\boldsymbol{\theta}_1^*$ (obtained after calibration) to estimate the solidification gradient and speed of the solidification

Table 2 Specifications of the PF model

The phase field model, $\mathcal{M}_2$	
Variable summary	
$\boldsymbol{x_2} = [S, G]^{\mathrm{T}}$	
$\boldsymbol{\theta_2} = [\sigma, M, p^{\mathrm{int}}]^{\mathrm{T}}$	
$\boldsymbol{y_2} = [\lambda, k_V]^{\mathrm{T}}$	
Control inputs, $\mathbf{x}_2$	
S: Solidification speed	(m/s)
G: Solidification gradient	(K/m)
Model parameters, $\boldsymbol{\theta}_2$	
σ: Interface energy	(J/cm^2)
M : Interface mobility	(cm^4/Js)
p^{int}: Interface permeability	(cm^3/Js)
Outputs, $\mathbf{y}_2$	
λ: PDAS	(μm)
k_V: Velocity dependent partition coefficient	

tail, namely, G_0 and S_0 , respectively. Then G_0 and S_0 constitute the input vector $\mathbf{x}_2$ as described in Table 2. We can then use the trained GP surrogate model and input $\mathbf{x}_2$ and $\boldsymbol{\theta}_2^*$ to estimate the simulation outputs of primary dendrite arm spacing λ.

We draw the reader's attention to challenges that are addressed using our proposed framework. Recall that both the FETM and PF models have sets of parameters that need to be calibrated in order to predict the primary dendrite arm spacing, as described in the previous paragraph. To conduct parameter calibration, experimental observations are needed. However, out of the six different outputs of the FETM (W, D, L, T_0, S_0, G_0), only the melt pool width and depth (W and D) are practical to measure. Although the FETM can be calibrated independently using melt pool width and depth, there is no guarantee that the predicted unmeasurable outputs (in particular, solidification gradients) will be accurate and result in satisfactory PDAS predictions. Furthermore, the PF model cannot even be independently calibrated because the inputs are not experimentally measurable. In other words, our proposed framework in Sec. 3 serves two purposes: (1) it enables better calibration and predictive power of the FETM, and (2) it enables the calibration of the PF model with inputs of great uncertainty.

3 Bayesian Calibration for Coupled Simulation Models

We first start by important terminology disambiguation: since the majority of ICME models for AM are implemented using computer codes, we will use the terms computer model and simulation model interchangeably throughout the remainder of the paper. In this section, we describe the framework for the hierarchical calibration of simulation models. First, in Sec. 3.1 we construct surrogates for the physics-based models. Next, in Sec. 3.2 we describe how to handle the challenging case of conducting calibration when unmeasurable variables are involved in the coupled models.

3.1 Surrogate Models. The two models described in the Secs. 2.1 and 2.2 are computationally expensive, each $\mathcal{M}_1$ run takes an average of 5 min and a $\mathcal{M}_2$ run even costs approximately 4 h. To enable using these models for effectively establishing the desired PS(PP) relationships—we note that we have yet to attempt to connect the resulting microstructure models to predictions of material properties but this can potentially be done through other approaches (see, for example, Refs. [53] and [54])—and effectively conducting uncertainty quantification and calibration analysis, we replace the simulation models with fast GP surrogates in the form of Python objects. In fact, directly coupling physics-based computer simulation codes can be extremely difficult. Examples of using surrogates for coupling multiple simulation models can be found in previous literature studies [40,55].

To build GP surrogates for the two models, we use Latin hypercube sampling with 100–200 sample size (depending on the simulations run time) to generate simulations from the computer models that will be used to train the GPs. Since the two models $\mathcal{M}_1$ and $\mathcal{M}_2$ have multiple outputs, one can also use multi-output GP surrogate models to replace the models with a fast surrogate, see, for example, Ref. [47]. However, for simplicity, we use multiple independent GP surrogates for each model instead of building a single multi-output GP. When constructing surrogate models, we use the Matérn covariance function $C_\nu(d)$ in which the covariance between two points separated by d distance units is given by

$$C_\nu(d) = \frac{2^{1-\nu}}{\Gamma(\nu)}\left(\frac{\sqrt{2\nu}d}{l}\right)^{\nu} K_\nu\left(\frac{\sqrt{2\nu}d}{l}\right) \tag{6}$$

$$d = \sqrt{(\mathbf{x}_i - \mathbf{x}_j)^{\top} \cdot (\mathbf{x}_i - \mathbf{x}_j)} \tag{7}$$

where d is the Euclidean distance, Γ is the gamma function, K_ν is the modified Bessel function of the second kind, and l and ν are non-negative parameters of the covariance. The Matérn covariance structure is a more flexible function than the commonly used squared exponential kernel, making it suitable for representing many physical and engineering systems. In our surrogate models training, we choose $\nu = 1.5$ which is common practice in machine learning as it guarantees differentiability [56].

Next, we use the computer simulation runs to estimate the hyperparameters of GP surrogate models for $\mathcal{M}_1$ and $\mathcal{M}_2$. Two GPs are needed for $\mathcal{M}_1$: one for predicting melt pool width (W), which is the observable response; and another GP for solidification gradient at the tail (G_0), which is unmeasurable. Note that, since the solidification tail is the very last point on the melt pool solidification front, its solidification speed (S_0) equals the laser scan speed, hence $S_0 = v$, which means there is no need to build a surrogate model for S_0. One additional GP is needed for $\mathcal{M}_2$ for predicting primary dendrite arm spacing (λ) at the melt pool solidification tip. Finally, we use the mean absolute percentage error (MAPE) as our performance metric, which is defined as

$$\mathrm{MAPE} = \frac{1}{N}\sum_{i=1}^{N}\left|\frac{y_i^S - \hat{y}_i^S}{y_i^S}\right| \times 100\% \tag{8}$$

where y_i^S is the output of the simulation model at input $(\mathbf{x}, \boldsymbol{\theta})_i$ and $\hat{y}_i^S$ is the prediction evaluated at the same input $(\mathbf{x}, \boldsymbol{\theta})_i$.

3.2 Multilevel Calibration. For a network of hierarchical models, a possible approach for conducting calibration (and uncertainty quantification in general) is through the Bayesian network (BN) [40,43,57]. BN is a tool that captures relationships between the variables and parameters within a network of models using a directed acyclic probabilistic graph [58]. Establishing PSPP relationships in LPBF involves the use of multiple hierarchically linked computational material models. Systematic calibration and uncertainty quantification of model parameters for this network of models is an essential task to enable the usability of these models to guide process design and optimization [31]. The system in hand can be constructed using two hierarchical models $\mathcal{M}_1$ and $\mathcal{M}_2$ as follows: the first model $\mathcal{M}_1$ takes vectors $\mathbf{x}_1$ and $\boldsymbol{\theta}_1$ as the control inputs and calibration parameters, respectively. The outputs of $\mathcal{M}_1$ are partitioned into two distinct vectors, measurable $\hat{\mathbf{y}}_{1Q}$ (W in Table 1) and unmeasurable $\hat{\mathbf{y}}_{1U}$ (S_0 and G_0 in Table 1). For $\hat{\mathbf{y}}_{1Q}$, there exists an experimental dataset $\boldsymbol{D}_{1Q}$, which is a collection of control input matrix $\boldsymbol{X}_{1Q}^E$ and the corresponding observed responses $\boldsymbol{Y}_{1Q}^E$. The second model $\mathcal{M}_2$ takes $\hat{\mathbf{y}}_{1U}$ as inputs and $\boldsymbol{\theta}_2$ as the calibration parameters. The output of $\mathcal{M}_2$ is the vector $\boldsymbol{y}_2$, which is observed by the dataset $\boldsymbol{D}_2$. Similarly, $\boldsymbol{D}_2$ is the collection of $\boldsymbol{X}_2^E$ and $\boldsymbol{Y}_2^E$. The Bayesian network for the two-model system is shown in Fig. 5.

In the network shown in Fig. 5, we have also added an additional set of nodes ϵ, δ, ψ, σ for each model. These nodes serve to

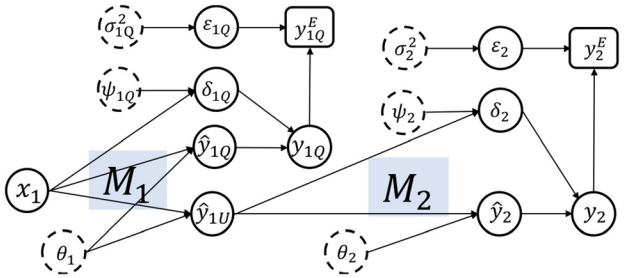

Fig. 5 Bayesian network for FETM-PF coupled simulation models

fulfill the well-established procedure of Bayesian calibration proposed in the seminal paper [37]. More specifically, for each dataset $\boldsymbol{D}_{(\cdot)}$, the node $\epsilon_{(\cdot)}$ represents a zero-mean independently distributed Gaussian noise to account for measurement error in the dataset. The hyperparameter for this node is denoted by $\sigma^2_{(\cdot)}$. Additionally, Kennedy and O'Hagan [37] require a model discrepancy function $\boldsymbol{\delta}_{(\cdot)}$ with the hyperparameter vector $\psi_{(\cdot)}$. The discrepancy function (sometimes known as model bias) refers to missing physics in the simulation model, see Ref. [47] for more details. The fundamental statistical calibration models for the system are

$$\mathbf{y}^E_{1Q} = \hat{\mathbf{y}}_{1Q}(\mathbf{x}_1;\boldsymbol{\theta}_1) + \boldsymbol{\delta}_{1Q}(\mathbf{x}_1) + \boldsymbol{\epsilon}_{1Q} \tag{9}$$

$$\mathbf{y}^E_2 = \hat{\mathbf{y}}_2\left(\hat{\mathbf{y}}_{1U};\boldsymbol{\theta}_2\right) + \boldsymbol{\delta}_2\left(\hat{\mathbf{y}}_{1U}\right) + \boldsymbol{\epsilon}_2 \tag{10}$$

Here, we assume the unknown regression parameter ρ in the canonical calibration model of [37] as 1, and the discrepancy function $\boldsymbol{\delta}_{(\cdot)}$ follows a Gaussian process with zero mean and a squared exponential (SE) covariance as follows:

$$\boldsymbol{\delta}_{(\cdot)} \sim \mathbf{GP}(\mathbf{0}, \boldsymbol{\Sigma}_{(\cdot)}) \tag{11}$$

$$\begin{aligned}\boldsymbol{\Sigma}_{(\cdot)} &= \left[C_{(\cdot)}(\mathbf{x}_i,\mathbf{x}_j)\right]_{i,j} \\ &= \left[\sigma^2_{(\cdot),\delta}\exp\left(-\frac{(\mathbf{x}_i-\mathbf{x}_j)^\top(\mathbf{x}_i-\mathbf{x}_j)}{2\ell^2_{(\cdot),\delta}}\right)\right]_{i,j}\end{aligned} \tag{12}$$

where $C_{(\cdot)}(\cdot,\cdot)$ is the SE covariance function with variance parameter $\sigma^2_{(\cdot),\delta}$ and lengthscale parameters vector $\boldsymbol{\ell}_{(\cdot),\delta}$. $\mathbf{x}_i$ is control input for models, for $\mathcal{M}_1$ $\mathbf{x}_i$ is consisted of P and v, for $\mathcal{M}_2$ $\boldsymbol{x}_i$ is consisted of S_0 and G_0. We denote the tuple of hyperparameters with $\boldsymbol{\psi}_{(\cdot)} = (\sigma^2_{(\cdot),\delta}, \boldsymbol{\ell}_{(\cdot),\delta})$. The goal is to use the available data ($\boldsymbol{D}_{1Q}$ and $\boldsymbol{D}_2$) to make inference about the hyperparameters $\boldsymbol{\psi}_{(\cdot)}$ and $\sigma^2_{(\cdot)}$ such that both models offer reasonable predictions.

It is convenient to define network parameters $\boldsymbol{\Phi}_1 = \left\{\sigma^2_{1Q}, \boldsymbol{\psi}_{1Q}, \boldsymbol{\theta}_1\right\}$ and $\boldsymbol{\Phi}_2 = \left\{\sigma^2_2, \boldsymbol{\psi}_2, \boldsymbol{\theta}_2\right\}$. By definition, the joint probability distribution of the network $f(\mathcal{U})$ is given by

$$f(\mathcal{U}) = \pi(\boldsymbol{\Phi}_1,\boldsymbol{\Phi}_2)\mathcal{L}(\mathbf{y}_{\mathbf{D}_{1Q}}, \mathbf{y}_{\mathbf{D}_2}|\boldsymbol{\Phi}_1,\boldsymbol{\Phi}_2) \tag{13}$$

where $\mathcal{L}(\mathbf{y}_{\mathbf{D}_{1Q}}, \mathbf{y}_{\mathbf{D}_2}|\boldsymbol{\Phi}_1,\boldsymbol{\Phi}_2)$ is the joint likelihood of the available experimental datasets, i.e., $\boldsymbol{D}_{1Q}$ and $\boldsymbol{D}_2$, $\pi(\boldsymbol{\Phi}_1,\boldsymbol{\Phi}_2)$ is the prior probability density function of the network parameters. Given the network parameters $\boldsymbol{\Phi}_1, \boldsymbol{\Phi}_2$, we assume independent observations for $\mathbf{y}_{1Q}$ and $\mathbf{y}_2$, and also independence of the parameters $\boldsymbol{\Phi}_1$ and $\boldsymbol{\Phi}_2$

$$\mathcal{L}(\mathbf{y}_{\mathbf{D}_{1Q}}, \mathbf{y}_{\mathbf{D}_2}|\boldsymbol{\Phi}_1,\boldsymbol{\Phi}_2) = \mathcal{L}(\mathbf{y}_{\mathbf{D}_{1Q}}|\boldsymbol{\Phi}_1)\mathcal{L}(\mathbf{y}_{\mathbf{D}_2}|\boldsymbol{\Phi}_1,\boldsymbol{\Phi}_2) \tag{14}$$

$$\pi(\boldsymbol{\Phi}_1,\boldsymbol{\Phi}_2) = \pi(\boldsymbol{\Phi}_1)\pi(\boldsymbol{\Phi}_2) \tag{15}$$

From Bayes' formula, it follows that the posterior probability density function of $(\boldsymbol{\Phi}_1,\boldsymbol{\Phi}_2)$ is proportional to the joint probability distribution of the network. However, simultaneously calibrating two coupled models can create a computational burden, Urbina et al. [40] proposed the segmented calibration method. Therefore, we have

$$\begin{aligned}P(\boldsymbol{\Phi}_1,\boldsymbol{\Phi}_2|\mathbf{y}_{\mathbf{D}_{1Q}}, \mathbf{y}_{\mathbf{D}_2}) &\propto f(\mathcal{U}) \\ &\propto \mathcal{L}(\mathbf{y}_{\mathbf{D}_{1Q}}|\boldsymbol{\Phi}_1)\mathcal{L}(\mathbf{y}_{\mathbf{D}_2}|\boldsymbol{\Phi}_1,\boldsymbol{\Phi}_2) \\ &\approx \mathcal{L}(\mathbf{y}_{\mathbf{D}_{1Q}}|\boldsymbol{\Phi}_1)\mathcal{L}(\mathbf{y}_{\mathbf{D}_2}|\boldsymbol{\Phi}_{1|\mathbf{D}_{1Q}},\boldsymbol{\Phi}_2)\end{aligned} \tag{16}$$

in which $\boldsymbol{\Phi}_{1|\boldsymbol{D}_{1Q}}$ denotes the posterior of $\boldsymbol{\Phi}_1$ from the first calibration. By isolating important relationships in the multilevel Bayesian network, this method can help reduce the calibration burden.

Given the joint probability distribution of the network, the posterior probability distribution of the network parameters, $\boldsymbol{\Phi}_1$ and $\boldsymbol{\Phi}_2$, can be obtained using the Hamiltonian Monte Carlo (HMC) method proposed by Duane et al. [59]. In high-dimensional distribution sampling, the random walk strategy of Metropolis-Hastings will result in poor mixing and low efficiency, and HMC is our ideal tool for its remarkable sampling efficiency. After the first network parameter $\boldsymbol{\Phi}^*_{1|\boldsymbol{D}_{1Q}}$ is estimated, we can get the inputs for $\mathcal{M}_2$ using kriging

$$\mathbf{X}^P_2 = \hat{\mathbf{y}}_{1U}(\mathbf{X}^P;\boldsymbol{\theta}^*_1) \tag{17}$$

Consider that we are interested in predicting $\mathbf{y}_2$ for a new set of inputs $\boldsymbol{X}^P_2$. According to Eq. (9), the posterior distribution of $\mathbf{y}^E_2$ conditional on the network parameters $\boldsymbol{\Phi}^*_{1|\boldsymbol{D}_{1Q}}$ and $\boldsymbol{\Phi}^*_2$ is a Gaussian process. The output matrix $\boldsymbol{Y}^P_2$ is given by

$$\mathbb{E}[\mathbf{Y}^P_2|\mathbf{y}_{\mathbf{D}_2}, \boldsymbol{\Phi}^*_{1|\mathbf{D}_{1Q}}, \boldsymbol{\Phi}^*_2] = \boldsymbol{\mu}(\mathbf{X}^P_2) + \boldsymbol{\Sigma}^{PE}(\boldsymbol{\Sigma}^{EE})^{-1}(\mathbf{Y}^E_2 - \boldsymbol{\mu}(\mathbf{X}^E_2)) \tag{18}$$

where

$$\boldsymbol{\mu}(\mathbf{X}^{(\cdot)}_2) = \hat{\mathbf{y}}_2(\mathbf{X}^{(\cdot)}_2;\boldsymbol{\theta}^*_2) \tag{19}$$

$$\boldsymbol{\Sigma}^{PE} = [C_{\delta_2}(\mathbf{x}^P_i, \mathbf{x}^E_j;\boldsymbol{\Psi}^*)]\begin{matrix} i = 1\ldots N_P \\ j = 1\ldots N_2\end{matrix} \tag{20}$$

$$\boldsymbol{\Sigma}^{EE} = \boldsymbol{\Sigma}^{EE}_\epsilon + \boldsymbol{\Sigma}^{EE}_\delta \tag{21}$$

$$\boldsymbol{\Sigma}^{EE}_\epsilon = \sigma^2_2\mathbf{I}_{N_2} \tag{22}$$

$$\boldsymbol{\Sigma}^{EE}_\delta = [C_{\delta_2}\left(\mathbf{x}^E_i, \mathbf{x}^E_j;\boldsymbol{\Psi}^*\right)]\begin{matrix} i = 1\ldots N_2 \\ j = 1\ldots N_2\end{matrix} \tag{23}$$

In the above equations, N_P is the number of new prediction points, N_2 is the size of dataset $\boldsymbol{D}_2$, and Ψ^* is the posterior estimates for the hyperparameters set $\Psi = \{\sigma^2_{1Q}, \sigma^2_2, \psi_{1Q}, \psi_2\}$. In summary, after estimating the network parameters $\boldsymbol{\Phi}^*_{1|\boldsymbol{D}_{1Q}}$ and $\boldsymbol{\Phi}^*_2$, Eqs. (17)–(22) allow us to make predictions for $\mathcal{M}_2$ even though we do not have any calibration observations for the second model input $\hat{\mathbf{y}}_{1U}$. Finally, MAPE is used to evaluate the performance of $\boldsymbol{Y}^P_2$.

4 Case Study: Calibration for a NiNb Alloy

We now apply the framework presented in Sec. 3 to the case study involving AM of a binary nickel-niobium alloy using LPBF. This alloy serves as a binary surrogate for Inconel 625 as previously suggested by some previous works [60]. The goal is to predict niobium segregation during AM by hierarchically linking a finite element thermal model (Sec. 2.1) and a phase field microstructure model (Sec. 2.2). It is important to point out that in this work, we use experimental observations from processing custom fabricated nickel-niobium powder. This is in contrast to previous

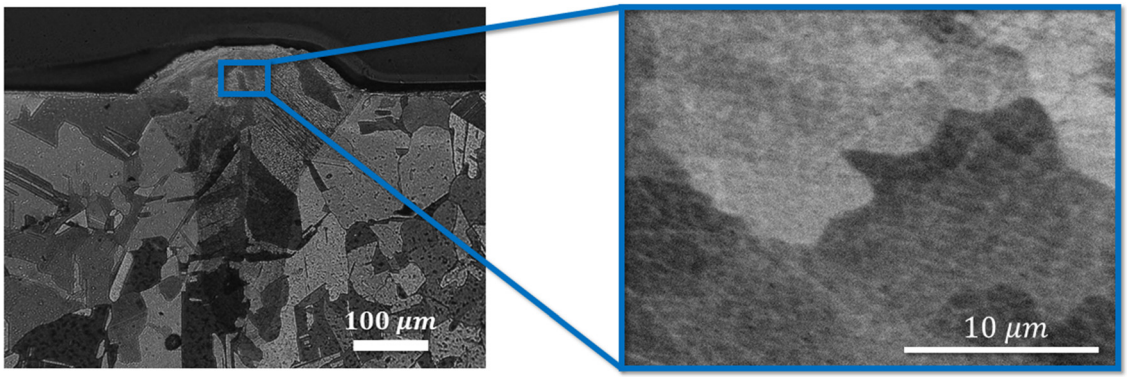

Fig. 6 Sample melt pool cross section and microstructure images for a representative single track; the melt pool cross section image (the left one) is taken using OM, while SEM is used to obtain the microstructure image (the right one) that shows segregation

works that generated simulations for nickel-niobium but conducted experimental validation using commercial Inconel powder. This mismatch between the alloy actually printed and the alloy used in the simulations makes it impossible to directly validate and verify the simulation schemes, as was shown by this collaboration [49].

4.1 Manufacturing Experiments and Material Characterization. Single tracks with 10 mm length and spaced 1 mm apart were printed using a commercial ProX DMP 200 LPBF system by 3D Systems (Rock Hill, SC) equipped with a Gaussian profile fiber laser with wavelength 1070 nm and beam size 80 μm. Argon was used as an inert protective atmosphere during fabrication. Gas atomized Ni-5 wt %Nb powder produced by Nanoval GmbH & Co. KG (Berlin, Germany) was used. Tracks were built on a Ni-5 wt %Nb base plate. Cross sections of the single tracks were cut using wire electrical discharge machining, and the specimens were polished down to 0.25 μm with water-based diamond suspension polishing solutions. Kalling's Solution No. 2 (5 g $CuCl_2$, 100 mL HCl, and 100 mL ethanol) was used to etch the Ni-5 wt %Nb single tracks to obtain optical micrographs.

Optical microscopy (OM) was carried out using a Keyence VH-X digital microscope equipped with a VH-Z100 wide range zoom lens. Width measurements were taken using the VH-X software. Three cross sections were measured for each track, and the width values were averaged from these measurements. Backscattered electron images of polished single tracks were captured at 15 kV and 30 nA. Backscattered electron images were processed using IMAGEJ software [61] in order to determine PDAS at different locations along select single tracks. The displayed PDAS values were averaged from 30 measurements at each location. Figure 6 shows sample OM and SEM images for a representative single track. The images demonstrate a transverse cross section of the melt pool. The microstructure can then be characterized using the SEM images and segregation can be quantified.

The experimental dataset $\boldsymbol{D}_{1Q}$ consists of 40 points and $\boldsymbol{D}_2$ has 11 points, which are experimental observations for $\mathcal{M}_1$ and $\mathcal{M}_2$, respectively. Each data point in $\boldsymbol{D}_{1Q}$ represents the melt pool width corresponding to a specific setting of process parameters for the Ni-5 wt %Nb alloy, and each point in $\boldsymbol{D}_2$ shows the primary dendrite arm spacing value under its process parameters. Figure 7 shows a plot of the experimental data for each of the two models in our study. Tables 4 and 5 in the Appendix present the whole experimental observations and train-test splitting in $\mathcal{M}_1$ and $\mathcal{M}_2$, respectively.

4.2 Building Surrogate Models. To train GP surrogate models, we need to obtain simulation training data first. Using the FETM and PF model described in Sec. 2, we generated 238 $\mathcal{M}_1$ simulations and 100 $\mathcal{M}_2$ simulation runs according to the Latin

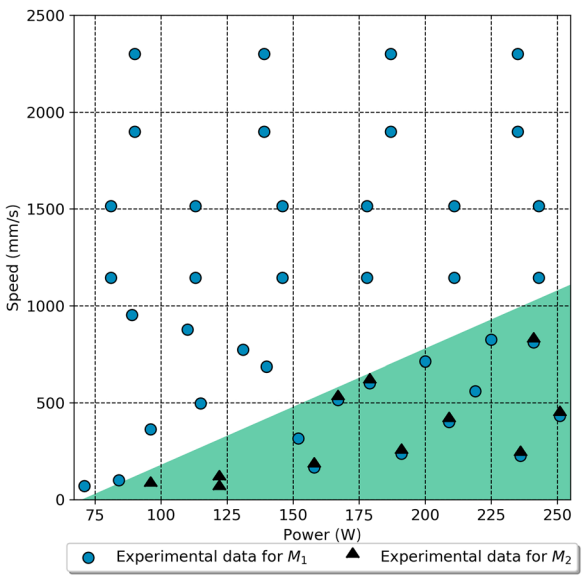

Fig. 7 Experimental data grid

hypercube sampling strategy. The simulation parameters boundaries: For $\mathcal{M}_1$, the control inputs vector $\mathbf{x}_1 = [P, v]^\top$ has bounds $\mathbf{x}_{1\,\min} = \{80, 0.050\}$ and $\mathbf{x}_{1\max} = \{250, 2.0\}$, and the calibration parameters vector $\boldsymbol{\theta}_1 = [K_s, K_L, K_{Lz}, K_V, K_{Vz}, A_0, A_{\max}]^\top$ is bounded between $\boldsymbol{\theta}_{1\,\min} = \{60, 100, 0.5, 5, 1000, 0.25, 0.6\}$ and $\boldsymbol{\theta}_{1\max} = \{100, 200, 1.5, 20, 2000, 0.4, 0.8\}$; For $\mathcal{M}_2$, the bounds for $\mathbf{x}_2 = [S_0, G_0]^\top$ are $\mathbf{x}_{2\,\min} = \{7 \times 10^6, 0.05\}$ and $\mathbf{x}_{2\max} = \{1.5 \times 10^7, 0.60\}$, and $\boldsymbol{\theta}_2 = [\sigma, M, p^{\text{int}}]^\top$ is bounded between $\boldsymbol{\theta}_{2\,\min} = \{6 \times 10^{-7}, 4, 5000\}$ and $\boldsymbol{\theta}_{2\max} = \{4 \times 10^{-6}, 11, 30, 000\}$. For brevity, the units are omitted readers can find them in Tables 1 and 2.

Python default optimizer was used which employs the L-BFGS-B algorithm developed by Byrd et al. [62]. To evaluate the predictive accuracy of the GP surrogates, k-fold cross-validation was conducted. Since values of G_0 are large, we trained a GP surrogate for $\ln G_0$. Figures 8(*a*) and 8(*b*) show the results of 17-fold cross-validation for melt pool width (W) and the logarithm of solidification gradient at the tail ($\ln G_0$), respectively. Figure 8(*c*) shows the result of 10-fold cross-validation for primary dendrite arm spacing (λ) at the melt pool solidification tip.

Note that in Fig. 8 plots, the horizontal axes represent the outputs of the simulation models, while the vertical axes show the predicted outputs using GP surrogates with bars representing 95% confidence intervals for these predictions. The orange line represents the ideal case with surrogate model predictions in full

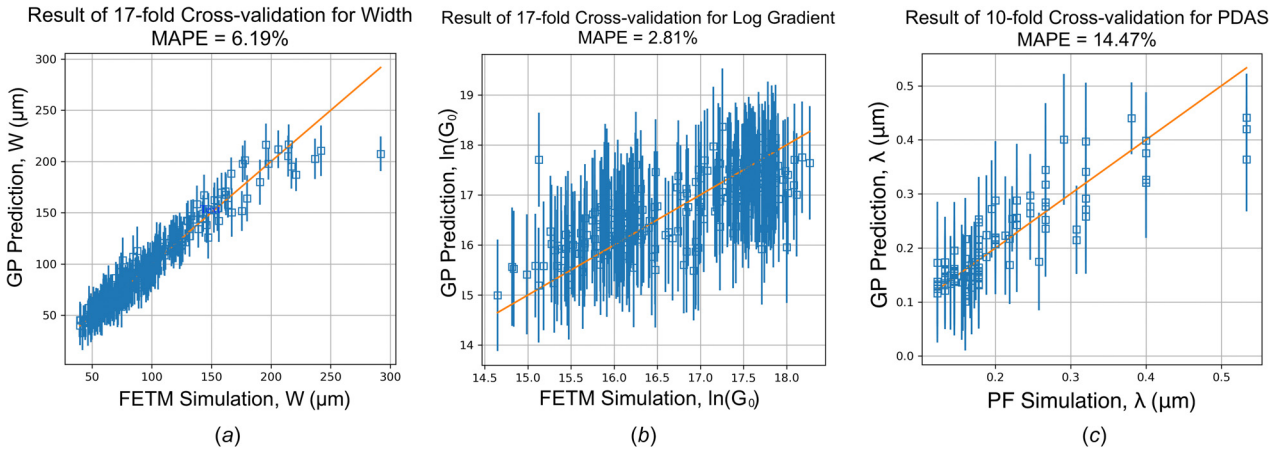

Fig. 8 Cross-validation of GP surrogates for (*a*) melt pool width, W, (*b*) logarithm of solidification gradient at the tail, $\ln G_0$, and (*c*) primary dendrite arm spacing, λ

agreement with computer model simulations. From the cross-validation figures and the reported MAPE at the top of each plot, it's fair to say that the predictive performance of the surrogate models is reasonable. In other words, the GP surrogate models represent good approximations that can be used in lieu of the original expensive computer models.

4.3 Multilevel Calibration. We employed the Bayesian approach to estimate the network calibration parameters, $\boldsymbol{\theta}_1$ and $\boldsymbol{\theta}_2$, and the set of hyperparameters, $\boldsymbol{\Psi} = \{\boldsymbol{\ell}_{1Q,\delta}, \sigma^2_{1Q,\delta}, \sigma^2_{1Q,\varepsilon}, \boldsymbol{\ell}_{2,\delta}, \sigma^2_{2,\delta}, \sigma^2_{2,\varepsilon}\}$, as introduced in Sec. 3.2. The following prior distributions were used:

$$\theta_i \sim \text{Beta}\left(1.1, 1.1, \alpha^{\theta_i}, \beta^{\theta_i}\right), \quad i = 1, \ldots, 7 \tag{24}$$

$$\ell_{\cdot,\delta,j} \sim \text{Log} - \text{Normal}\left(\mu = 0, \sigma^2 = \frac{1}{4}\right), \quad j = 1, \ldots, p \tag{25}$$

$$\sigma^2_{\cdot,\delta} \sim \text{Inverse} - \text{Gamma}(\alpha = 2, \beta = 1) \tag{26}$$

$$\sigma^2_{\cdot,\epsilon} \sim \text{Inverse} - \text{Gamma}(\alpha = 2, \beta = 1) \tag{27}$$

where α^{θ_i}, β^{θ_i} indicate θ_i's lower and upper bounds for the non-standard beta distributions (see the ranges in Table 3) as recommended by the domain expert. For the $p_\cdot$-dimensional lengthscale parameter vector, $\boldsymbol{\ell}_{\cdot,\delta}$, log-normal priors were used in each dimension of inputs since the log-normal distribution has positive support. $p_\cdot$ is the number of control inputs dimension in dataset $\boldsymbol{D}_\cdot$. For the variance parameters $\sigma^2_{\cdot,\delta}$ and $\sigma^2_{\cdot,\varepsilon}$ inverse gamma priors were selected because they represent conjugate priors for the multivariate normal likelihood function in our model. Note that the priors for the calibration parameters $\theta_\cdot$ were set as flat beta distributions to avoid any bias in estimation. Although it is common practice to choose uniform priors when little information is known about the parameters beyond their estimated minimum and maximum values, in high-dimensional Markov Chain Monte Carlo (MCMC) uniform priors may result in posterior density overstack on the boundaries. Readers who are interested in how to construct informative prior distributions using additional prior knowledge can find more details in Refs. [63] and [64].

Table 3 Posterior estimates of calibration parameters

Parameter	Range	Estimate	Unit
$\mathcal{M}_1$: $\boldsymbol{\theta}_1$			
K_S	[60, 100]	68.04	(W/mK)
K_L	[100, 200]	149.75	(W/mK)
KLz	[0.5, 1.5]	1.29	(W/mK)
K_V	[5, 20]	12.995	(W/mK)
$KV\,z$	[1000, 2000]	1361.47	(W/mK)
A_0	[0.25, 0.4]	0.34	
$A\max$	[0.6, 0.8]	0.73	
$\mathcal{M}_2$: $\boldsymbol{\theta}_2$			
σ	$[6 \times 10^{-7}, 4 \times 10^{-6}]$	1.11×10^{-7}	(J/cm^2)
M	[4, 11]	10.02	(cm^4/Js)
p^{int}	[5000, 30,000]	9107.01	(cm^3/Js)

Using HMC, the posterior distributions of the calibration parameters ($\boldsymbol{\theta}_1$ and $\boldsymbol{\theta}_2$) and hyperparameters ($\boldsymbol{\Psi}$) were evaluated after a 1000 burn-in period and thinning every tenth sample. Implementation and programing were done in Python version 3.7.11 and PyMC3 version 3.11.2. Figures 9 and 10 show the histograms and kernel density estimates of the posterior distributions and the prior distributions for the calibration parameters in model $\mathcal{M}_1$ and $\mathcal{M}_2$, respectively. We use the maximum posterior probability estimates, i.e., posterior modes, as the posterior estimates for calibration parameters.

Table 3 lists the lower and upper bounds for each calibration parameter in addition to the final estimates (modes of the posterior distributions) after the Bayesian calibration. Using the posterior estimates from Table 3, we can predict the QoI (i.e., PDAS) of the two-model coupled system. In Fig. 11(*a*), the experimental data for training are shown in blue and mean prediction points for test data are in red, in (b) the abscissa is the experimental observation while the ordinate shows the posterior mean prediction at the squared marker. The confidence interval bars are ± 1.96 standard error of prediction SE_{pred}, which is computed by

$$\text{SE}_{\text{pred}} = \sqrt{\frac{\sum_{i=1}^{n_{\text{pred}}} \left(\mathbf{Y}_{\text{obs,i}} - \mathbf{Y}_{\text{pred,i}}\right)^2}{n_{\text{pred}}}} \tag{28}$$

where $\boldsymbol{Y}_{\text{obs,i}}$ is the ith experimental observation from the test dataset, $\boldsymbol{Y}_{\text{pred,i}}$ is the ith posterior mean prediction, and n_{pred} is the number of test data points (three in our case). The standard error of PDAS prediction was calculated as 0.023 μm.

4.4 Sensitivity Analysis. To quantify the effect of input parameters of the coupled models in this study, we conducted the formal variance-based sensitivity analysis through Sobol indices. The main idea is to compare the responses of our calibrated model based on two different datasets of size N. We followed the formulation presented in Ref. [65], the total sensitivity index for a subset u of variables $\boldsymbol{x}_u \subseteq \boldsymbol{x}$ is

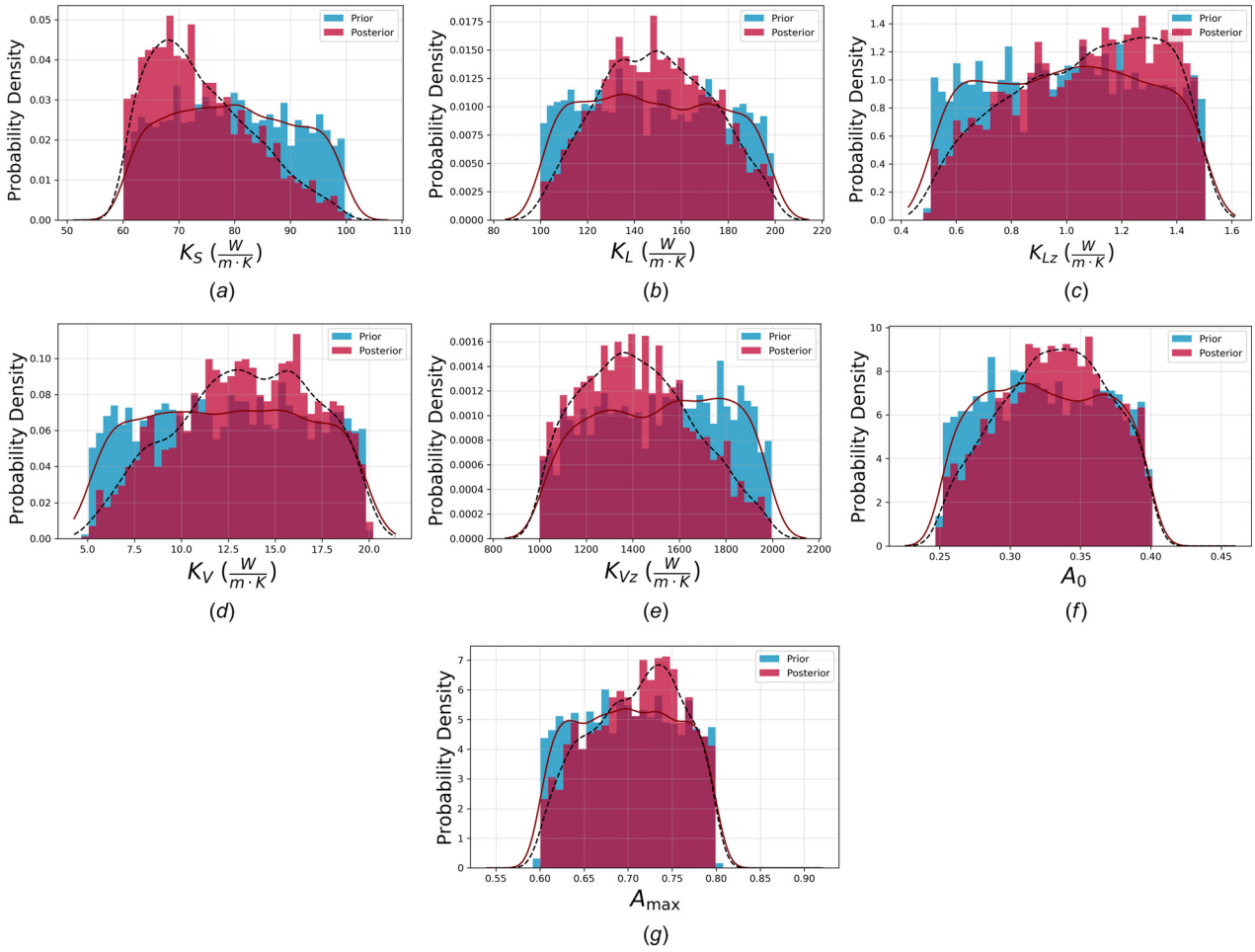

Fig. 9 Histograms and kernel density estimates of the prior and posterior distributions for the FETM calibration parameters, from (*a*) to (*g*) are K_s, K_L, K_{Lz}, K_V, K_{Vz}, A_0, and A_{max}, respectively

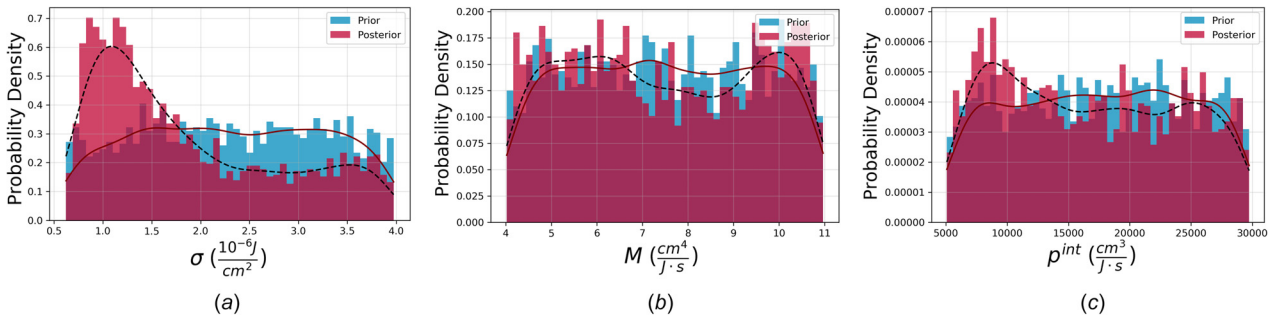

Fig. 10 Histograms and kernel density estimates of the prior and posterior distributions for the PF model calibration parameters, from (*a*) to (*c*) are σ, M, and p^{int}, respectively

$$\hat{\bar{\kappa}}_u^2 = \frac{1}{2N}\sum_{i=1}^{N}\left(f\left(\mathbf{x}_i^{(1)}\right) - f\left(\mathbf{x}_{i,-u}^{(1)} : \mathbf{x}_{i,u}^{(2)}\right)\right)^2 \tag{29}$$

where $\boldsymbol{x}_i^{(1)}, \boldsymbol{x}_i^{(2)} \sim \mathrm{U}(\mathcal{X})$, $\mathcal{X}$ is the working region for $\mathcal{M}_2$ (the green area in Fig. 7), and $\boldsymbol{x}_{i,-u}^{(1)} : \boldsymbol{x}_{i,u}^{(2)}$ represents that in ith points, the jth variable of $\boldsymbol{x}$ should equal $x_j^{(2)}$ if $j \in u$, otherwise $x_j^{(1)}$ if $j \notin u$.

For our two-level system, there are only two inputs, we define the total sensitivity index for P and v by

$$\hat{\bar{\kappa}}_P^2 = \frac{1}{2N}\sum_{i=1}^{N}\left(f\left(P_i^{(1)}, v_i^{(1)}\right) - f\left(P_i^{(2)}, v_i^{(1)}\right)\right)^2 \tag{30}$$

$$\hat{\bar{\kappa}}_v^2 = \frac{1}{2N}\sum_{i=1}^{N}\left(f\left(P_i^{(1)}, v_i^{(1)}\right) - f\left(P_i^{(1)}, v_i^{(2)}\right)\right)^2 \tag{31}$$

Using the posterior modes of calibration parameters in $\mathcal{M}_1$ and $\mathcal{M}_2$, we calculated the total sensitivity indices for P and v as

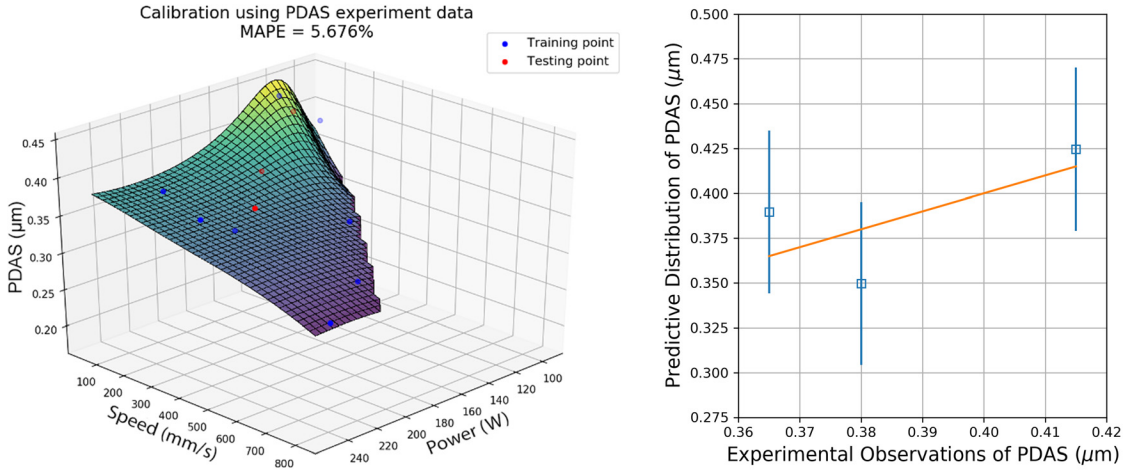

Fig. 11 Posterior predictive distribution for calibrated coupled surrogate models: (*a*) posterior mean estimates for PDAS and (*b*) PDAS posterior predictions with 95% confidence interval

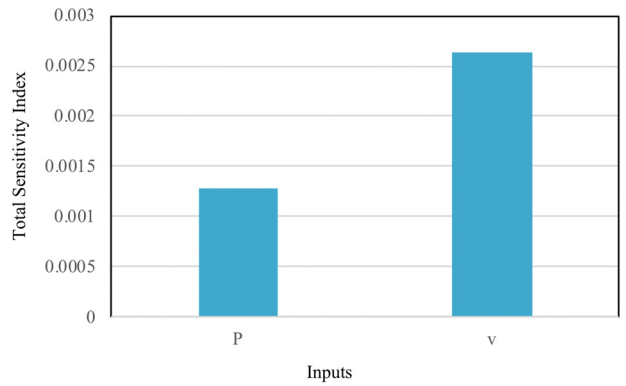

Fig. 12 Sensitivity analysis for the calibrated coupled models

visualized in Fig. 12. Therefore for the two-level coupled models in the study, laser speed v dominates the variance of the system.

5 Discussion and Conclusion

In this work, we present how to conduct rigorous calibration and uncertainty quantification analysis in a network of hierarchically coupled computational models. The network of coupled models is used to establish the process–microstructure–property–performance relationships in LPBF metal AM. The proposed framework is based on the use of a Bayesian network that enables modeling the relationships between models and capturing correlations and dependencies between their inputs and outputs. Furthermore, the BN framework allows the use of fast Gaussian process surrogate models to efficiently explore PSPP relationships over large input parameter spaces of the LPBF AM process.

It is worth noting that different models have different working regions, only after fully understanding the working region for each model can we successfully gather experimental data for calibration and UQ purposes. In our case study, we notice that the segregation phenomenon of the PF model only occurs in a small specific region of the input parameter space $\mathcal{X}$ (bounded $\mathcal{X}_{\min} = \{80\,\mathrm{W}, 0.05\,\mathrm{m/s}\}$, $\mathcal{X}_{\max} = \{250\,\mathrm{W}, 2.0\,\mathrm{m/s}\}$), which is characterized by high laser power and low laser speed, i.e., the green region in Fig. 7. Moreover, the time and effort in acquiring experimental data needed to calibrate different models are highly variable and dependent on the nature of the phenomenon being simulated. Therefore, in our case study, while we were capable of generating 40 experimental data points for the melt pool width (output of the FETM), only 11 experimental data points for the primary dendrite arm spacing (output of the PF model) were acquired. A side effect of the smaller experimental dataset for $\mathcal{M}_2$ could be numerical instability when conducting MCMC and estimating parameters and hyperparameters. In practice, it is recommended that the samples generated using MCMC should be treated with care: best practices regarding burn-in and thinning should be followed. Additionally, multiple runs of the entire MCMC should be conducted in order to avoid anomalous estimates. If further improvement to the accuracy of the calibrated PF model is desired, one needs to generate more observation data from its working region.

The contributions of the proposed work can be summarized as follows. First, we address the problem of conducting uncertainty quantification through a network of models (as opposed to a single model) in metal AM. Second, our framework enables conducting calibration even for surrogate models with inputs of great uncertainty. Finally, we validate our proposed framework using a case study from the LPBF of a binary nickel-niobium (NiNb) alloy. In contrast to previous works in the literature, we generate simulation and experimental data from the same material system to ensure the integrity of our validation efforts.

The case study involved a FETM for simulating the thermal history, hierarchically linked with a PF model for simulating Nb segregation during LPBF. Our results indicate very good predictive accuracy of the calibrated PF model, with the mean absolute percentage error of approximately 5.7% on test data. This work represents a building block to enable accurate and accelerated model-based qualification and certification of metal AM materials.

Funding Data

- United States Army Research Office (Grant No. W911NF-18-1-0278; Funder ID: 10.13039/100000183).
- National Science Foundation (Grant Nos. CMMI-1846676 and DGE-1545403; Funder ID: 10.13039/100000147).

Appendix: Experimental Data

Table 4 Experimental observations for $\mathcal{M}_1$

Sample	Power (W)	Speed (m/s)	Width (μm)
Training			
1	81	1.145	59.73
2	81	1.515	53.34
3	84	0.100	152.85
4	89	0.953	66.94
5	90	1.900	47.84
6	90	2.300	45.21
7	96	0.364	108.40
8	110	0.877	68.82
9	113	1.145	67.23
10	113	1.515	60.63
11	115	0.497	98.43
12	131	0.774	81.04
13	139	1.900	60.56
14	140	0.687	94.75
15	146	1.515	56.93
16	152	0.316	141.75
17	158	0.167	206.58
18	167	0.515	123.43
19	178	1.515	60.22
20	179	0.602	121.06
21	187	2.300	58.27
22	200	0.714	123.03
23	209	0.402	151.16
24	211	1.515	68.08
25	225	0.825	111.67
26	235	1.900	56.63
27	235	2.300	59.27
28	236	0.226	210.11
29	243	1.145	87.60
30	243	1.515	76.96
Test			
31	71	0.070	122.43
32	191	0.238	186.83
33	219	0.560	125.78
34	241	0.811	117.57
35	251	0.433	154.17
36	146	1.145	75.04
37	178	1.145	62.69
38	211	1.145	71.13
39	139	2.300	52.69
40	187	1.900	62.55

Table 5 Experimental observations for $\mathcal{M}_2$

Sample	Power (W)	Speed (m/s)	PDAS (μm)
Training			
1	179	0.602	0.290
2	251	0.433	0.397
3	96	0.067	0.383
4	241	0.811	0.310
5	167	0.515	0.350
6	191	0.238	0.316
7	122	0.050	0.430
8	236	0.226	0.396
Test			
9	158	0.167	0.365
10	209	0.402	0.380
11	122	0.100	0.415

References

[1] Parthasarathy, J., Starly, B., and Raman, S., 2011, "A Design for the Additive Manufacture of Functionally Graded Porous Structures With Tailored Mechanical Properties for Biomedical Applications," J. Manuf. Process., **13**(2), pp. 160–170.

[2] Muller, P., Mognol, P., and Hascoet, J.-Y., 2013, "Modeling and Control of a Direct Laser Powder Deposition Process for Functionally Graded Materials (Fgm) Parts Manufacturing," J. Mater. Process. Technol., **213**(5), pp. 685–692.

[3] Tapia, G., and Elwany, A., 2014, "A Review on Process Monitoring and Control in Metal-Based Additive Manufacturing," ASME J. Manuf. Sci. Eng., **136**(6), p. 060801.

[4] Spears, T. G., and Gold, S. A., 2016, "In-Process Sensing in Selective Laser Melting (Slm) Additive Manufacturing," Integrat. Mater. Manuf. Innov., **5**(1), pp. 16–40.

[5] Tolosa, I., Garciandía, F., Zubiri, F., Zapirain, F., and Esnaola, A., 2010, "Study of Mechanical Properties of Aisi 316 Stainless Steel Processed by "Selective Laser Melting", Following Different Manufacturing Strategies," Int. J. Adv. Manuf. Technol., **51**(5–8), pp. 639–647.

[6] Garibaldi, M., Ashcroft, I., Simonelli, M., and Hague, R., 2016, "Metallurgy of High-Silicon Steel Parts Produced Using Selective Laser Melting," Acta Mater., **110**, pp. 207–216.

[7] Mahmoudi, M., Elwany, A., Yadollahi, A., Thompson, S. M., Bian, L., and Shamsaei, N., 2017, "Mechanical Properties and Microstructural Characterization of Selective Laser Melted 17-4 ph Stainless Steel," Rapid Prototyp. J., **23**(2), pp. 280–294.

[8] Facchini, L., Vicente, N., Lonardelli, I., Magalini, E., Robotti, P., and Molinari, A., 2010, "Metastable Austenite in 17–4 Precipitation-Hardening Stainless Steel Produced by Selective Laser Melting," Adv. Eng. Mater., **12**(3), pp. 184–188.

[9] Li, S., Hassanin, H., Attallah, M. M., Adkins, N. J., and Essa, K., 2016, "The Development of Tini-Based Negative Poisson's Ratio Structure Using Selective Laser Melting," Acta Mater., **105**, pp. 75–83.

[10] Murr, L., Quinones, S., Gaytan, S., Lopez, M., Rodela, A., Martinez, E., Hernandez, D., Martinez, E., Medina, F., and Wicker, R., 2009, "Microstructure and Mechanical Behavior of Ti–6Al–4V Produced by Rapid-Layer Manufacturing, for Biomedical Applications," J. Mech. Behav. Biomed. Mater., **2**(1), pp. 20–32.

[11] El-Desouky, A., Carter, M., Mahmoudi, M., Elwany, A., and LeBlanc, S., 2017, "Influences of Energy Density on Microstructure and Consolidation of Selective Laser Melted Bismuth Telluride Thermoelectric Powder," J. Manuf. Process., **25**, pp. 411–417.

[12] Jia, Q., and Gu, D., 2014, "Selective Laser Melting Additive Manufacturing of Inconel 718 Superalloy Parts: Densification, Microstructure and Properties," J. Alloys Compd., **585**, pp. 713–721.

[13] Ma, J., Franco, B., Tapia, G., Karayagiz, K., Johnson, L., Liu, J., Arroyave, R., Karaman, I., and Elwany, A., 2017, "Spatial Control of Functional Response in 4D-Printed Active Metallic Structures," Sci. Rep., **7**(1), pp. 1–8.

[14] Tapia, G., Johnson, L., Franco, B., Karayagiz, K., Ma, J., Arroyave, R., Karaman, I., and Elwany, A., 2017, "Bayesian Calibration and Uncertainty Quantification for a Physics-Based Precipitation Model of Nickel–Titanium Shape-Memory Alloys," ASME J. Manuf. Sci. Eng., **139**(7), p. 071002.

[15] Elahinia, M., Moghaddam, N. S., Andani, M. T., Amerinatanzi, A., Bimber, B. A., and Hamilton, R. F., 2016, "Fabrication of Niti Through Additive Manufacturing: A Review," Prog. Mater. Sci., **83**, pp. 630–663.

[16] Bormann, T., Schumacher, R., Müller, B., Mertmann, M., and de Wild, M., 2012, "Tailoring Selective Laser Melting Process Parameters for Niti Implants," J. Mater. Eng. Perform., **21**(12), pp. 2519–2524.

[17] Haberland, C., Elahinia, M., Walker, J. M., Meier, H., and Frenzel, J., 2014, "On the Development of High Quality Niti Shape Memory and Pseudoelastic Parts by Additive Manufacturing," Smart Mater. Struct., **23**(10), p. 104002.

[18] Walker, J. M., Haberland, C., Taheri Andani, M., Karaca, H. E., Dean, D., and Elahinia, M., 2016, "Process Development and Characterization of Additively Manufactured Nickel–Titanium Shape Memory Parts," J. Intell. Mater. Syst. Struct., **27**(19), pp. 2653–2660.

[19] Kerwien, S., Collings, S., Liou, F., and Bytnar, M., 2013, *Measurement Science Roadmap for Metal-Based Additive Manufacturing*, National Institute of Standards and Technology, Gaithersburg, MD, Report. https://www.nist.gov/system/files/documents/el/isd/NISTAdd_Mfg_Report_FINAL-2.pdf

[20] Mani, M., Lane, B., Donmez, A., Feng, S., Moylan, S., and Fesperman, R., 2015, *Measurement Science Needs for Real-Time Control of Additive Manufacturing Powder Bed Fusion Processes*, NIST Interagency/Internal Report (NISTIR), National Institute of Standards and Technology, Gaithersburg, MD, [online].

[21] Seifi, M., Salem, A., Beuth, J., Harrysson, O., and Lewandowski, J. J., 2016, "Overview of Materials Qualification Needs for Metal Additive Manufacturing," JOM, **68**(3), pp. 747–764.

[22] Montazeri, M., Yavari, R., Rao, P., and Boulware, P., 2018, "In-Process Monitoring of Material Cross-Contamination Defects in Laser Powder Bed Fusion," ASME J. Manuf. Sci. Eng., **140**(11), p. 111001.

[23] Mahmoudi, M., Ezzat, A. A., and Elwany, A., 2019, "Layerwise Anomaly Detection in Laser Powder-Bed Fusion Metal Additive Manufacturing," ASME J. Manuf. Sci. Eng., **141**(3), p. 031002.

[24] Montazeri, M., and Rao, P., 2018, "Sensor-Based Build Condition Monitoring in Laser Powder Bed Fusion Additive Manufacturing Process Using a Spectral Graph Theoretic Approach," ASME J. Manuf. Sci. Eng., **140**(9), p. 091002.

[25] Imani, F., Gaikwad, A., Montazeri, M., Rao, P., Yang, H., and Reutzel, E., 2018, "Process Mapping and in-Process Monitoring of Porosity in Laser Powder Bed Fusion Using Layerwise Optical Imaging," ASME J. Manuf. Sci. Eng., **140**(10), p. 101009.
[26] Khairallah, S. A., Anderson, A. T., Rubenchik, A., and King, W. E., 2016, "Laser Powder-Bed Fusion Additive Manufacturing: Physics of Complex Melt Flow and Formation Mechanisms of Pores, Spatter, and Denudation Zones," Acta Mater., **108**, pp. 36–45.
[27] Megahed, M., Mindt, H.-W., N'Dri, N., Duan, H., and Desmaison, O., 2016, "Metal Additive-Manufacturing Process and Residual Stress Modeling," Integrat. Mater. Manuf. Innov., **5**(1), pp. 61–93.
[28] Zhang, D., Cai, Q., Liu, J., Zhang, L., and Li, R., 2010, "Select Laser Melting of w–ni–fe Powders: Simulation and Experimental Study," Int. J. Adv. Manuf. Technol., **51**(5–8), pp. 649–658.
[29] Masoomi, M., Thompson, S. M., and Shamsaei, N., 2017, "Laser Powder Bed Fusion of Ti-6Al-4V Parts: Thermal Modeling and Mechanical Implications," Int. J. Mach. Tools Manuf., **118–119**, pp. 73–90.
[30] National Research Council, 2008, *Integrated Computational Materials Engineering: A Transformational Discipline for Improved Competitiveness and National Security*, National Academies Press, Washington, DC.
[31] Hu, Z., and Mahadevan, S., 2017, "Uncertainty Quantification in Prediction of Material Properties During Additive Manufacturing," Scr. Mater., **135**, pp. 135–140.
[32] O'Hagan, A., 2006, "Bayesian Analysis of Computer Code Outputs: A Tutorial," Reliab. Eng. Syst. Saf., **91**(10–11), pp. 1290–1300.
[33] Chernatynskiy, A., Phillpot, S. R., and LeSar, R., 2013, "Uncertainty Quantification in Multiscale Simulation of Materials: A Prospective," Annu. Rev. Mater. Res., **43**(1), pp. 157–182.
[34] Panchal, J. H., Kalidindi, S. R., and McDowell, D. L., 2013, "Key Computational Modeling Issues in Integrated Computational Materials Engineering," Comput.-Aided Des., **45**(1), pp. 4–25.
[35] McDowell, D. L., and Kalidindi, S. R., 2016, "The Materials Innovation Ecosystem: A Key Enabler for the Materials Genome Initiative," MRS Bull., **41**(4), pp. 326–337.
[36] Trucano, T. G., Swiler, L. P., Igusa, T., Oberkampf, W. L., and Pilch, M., 2006, "Calibration, Validation, and Sensitivity Analysis: What's What," Reliab. Eng. Syst. Saf., **91**(10–11), pp. 1331–1357.
[37] Kennedy, M. C., and O'Hagan, A., 2001, "Bayesian Calibration of Computer Models," J. R. Stat. Soc. Ser. B (Stat. Methodol.), **63**(3), pp. 425–464.
[38] Conti, S., and O'Hagan, A., 2010, "Bayesian Emulation of Complex Multi-Output and Dynamic Computer Models," J. Stat. Plann. Infer., **140**(3), pp. 640–651.
[39] Higdon, D., Nakhleh, C., Gattiker, J., and Williams, B., 2008, "A Bayesian Calibration Approach to the Thermal Problem," Comput. Methods Appl. Mech. Eng., **197**(29–32), pp. 2431–2441.
[40] Urbina, A., Mahadevan, S., and Paez, T. L., 2012, "A Bayes Network Approach to Uncertainty Quantification in Hierarchically Developed Computational Models," Int. J. Uncertainty Quantif., **2**(2), pp. 173–193.
[41] Kyzyurova, K. N., Berger, J. O., and Wolpert, R. L., 2018, "Coupling Computer Models Through Linking Their Statistical Emulators," SIAM/ASA J. Uncertainty Quantif., **6**(3), pp. 1151–1171.
[42] Nagel, J. B., and Sudret, B., 2016, "A Unified Framework for Multilevel Uncertainty Quantification in Bayesian Inverse Problems," Probab. Eng. Mech., **43**, pp. 68–84.
[43] DeCarlo, E. C., Smarslok, B. P., and Mahadevan, S., 2016, "Segmented Bayesian Calibration of Multidisciplinary Models," AIAA J., **54**(12), pp. 3727–3741.
[44] Ghoreishi, S., and Allaire, D., 2017, "Adaptive Uncertainty Propagation for Coupled Multidisciplinary Systems," AIAA J., **55**(11), pp. 3940–11.
[45] Wang, Z., Liu, P., Ji, Y., Mahadevan, S., Horstemeyer, M. F., Hu, Z., Chen, L., and Chen, L.-Q., 2019, "Uncertainty Quantification in Metallic Additive Manufacturing Through Physics-Informed Data-Driven Modeling," JOM, **71**(8), pp. 2625–2634.
[46] Hu, Z., and Mahadevan, S., 2017, "Uncertainty Quantification and Management in Additive Manufacturing: Current Status, Needs, and Opportunities," Int. J. Adv. Manuf. Technol., **93**(5–8), pp. 2855–2874.
[47] Mahmoudi, M., Tapia, G., Karayagiz, K., Franco, B., Ma, J., Arroyave, R., Karaman, I., and Elwany, A., 2018, "Multivariate Calibration and Experimental Validation of a 3D Finite Element Thermal Model for Laser Powder Bed Fusion Metal Additive Manufacturing," Integrat. Mater. Manuf. Innov., **7**(3), pp. 116–135.
[48] Seede, R., Shoukr, D., Zhang, B., Whitt, A., Gibbons, S., Flater, P., Elwany, A., Arroyave, R., and Karaman, I., 2020, "An Ultra-High Strength Martensitic Steel Fabricated Using Selective Laser Melting Additive Manufacturing: Densification, Microstructure, and Mechanical Proper-Ties," Acta Mater., **186**, pp. 199–214.
[49] Karayagiz, K., Johnson, L., Seede, R., Attari, V., Zhang, B., Huang, X., Ghosh, S., Duong, T., Karaman, I., Elwany, A., and Arroyave, R., 2020, "Finite Interface Dissipation Phase Field Modeling of ni–nb Under Additive Manufacturing Conditions," Acta Mater., **185**, pp. 320–339.
[50] Karayagiz, K., Elwany, A., Tapia, G., Franco, B., Johnson, L., Ma, J., Karaman, I., and Arroyave, R., 2019, "Numerical and Experimental Analysis of Heat Distribution in the Laser Powder Bed Fusion of Ti-6Al-4V," IISE Trans., **51**(2), pp. 136–152.
[51] Steinbach, I., Zhang, L., and Plapp, M., 2012, "Phase-Field Model With Finite Interface Dissipation," Acta Mater., **60**(6–7), pp. 2689–2701.
[52] Zhang, L., and Steinbach, I., 2012, "Phase-Field Model With Finite Interface Dissipation: Extension to Multi-Component Multi-Phase Alloys," Acta Mater., **60**(6–7), pp. 2702–2710.
[53] Fernandez-Zelaia, P., Yabansu, Y. C., and Kalidindi, S. R., 2019, "A Comparative Study of the Efficacy of Local/Global and Parametric/Nonparametric Machine Learning Methods for Establishing Structure–Property Linkages in High-Contrast 3D Elastic Composites," Integrat. Mater. Manuf. Innov., **8**(2), pp. 67–15.
[54] Kalidindi, S. R., 2019, "A Bayesian Framework for Materials Knowledge Systems," MRS Commun., **9**(2), pp. 518–14.
[55] Stevens, G., Atamturktur, S., Lebensohn, R., and Kaschner, G., 2016, "Experiment-Based Validation and Uncertainty Quantification of Coupled Multi-Scale Plasticity Models," Multidis. Model. Mater. Struct., **12**(1), pp. 151–176.
[56] Rasmussen, C. E., and Williams, C. K. I., 2006, *Gaussian Processes for Machine Learning*, The MIT Press, Cambridge, MA.
[57] Ghanem, R., Higdon, D., and Owhadi, H., 2017, *Handbook of Uncertainty Quantification*, Springer, New York.
[58] Nielsen, T. D., and Jensen, F. V., 2009, *Bayesian Networks and Decision Graphs*, Springer, New York.
[59] Duane, S., Kennedy, A., Pendleton, B. J., and Roweth, D., 1987, "Hybrid Monte Carlo," Phys. Lett. B, **195**(2), pp. 216–222.
[60] Keller, T., Lindwall, G., Ghosh, S., Ma, L., Lane, B. M., Zhang, F., Kattner, U. R., Lass, E. A., Heigel, J. C., Idell, Y., Williams, M. E., Allen, A. J., Guyer, J. E., and Levine, L. E., 2017, "Application of Finite Element, Phase-Field, and Calphad-Based Methods to Additive Manufacturing of ni-Based Superalloys," Acta Mater., **139**, pp. 244–253.
[61] Rasband, W., 1997, *ImageJ*. Us National Institutes of Health, Bethesda, MD.
[62] Byrd, R. H., Lu, P., Nocedal, J., and Zhu, C., 1995, "A Limited Memory Algorithm for Bound Constrained Optimization," SIAM J. Sci. Comput., **16**(5), pp. 1190–1208.
[63] Boluki, S., Esfahani, M. S., Qian, X., and Dougherty, E. R., 2017, "Incorporating Biological Prior Knowledge for Bayesian Learning Via Maximal Knowledge-Driven Information Priors," BMC Bioinform., **18**(S14), p. 1.
[64] Boluki, S., Esfahani, M. S., Qian, X., and Dougherty, E. R., 2017, "Constructing Pathway-Based Priors Within a Gaussian Mixture Model for Bayesian Regression and Classification," IEEE/ACM Trans. Comput. Biol. Bioinform., **16**(2), pp. 524–537.
[65] Owen, A. B., 2013, "Variance Components and Generalized Sobol' Indices," SIAM/ASA J. Uncertainty Quantif., **1**(1), pp. 19–41.